J. Fluid Mech. (2022), *vol*. 936, A28, doi:10.1017/jfm.2021.1111

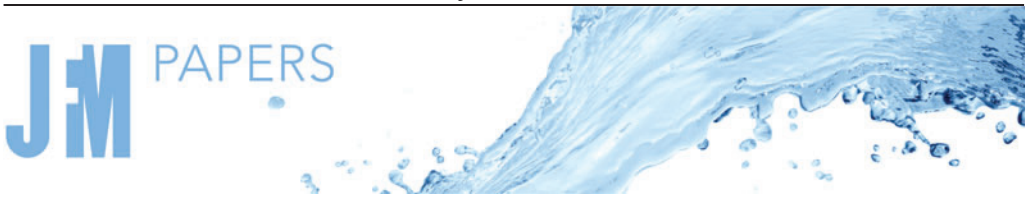

Shear-induced modulation on thermal convection over rough plates

Tian-Cheng Jin[1], **Jian-Zhao Wu**[1],†, **Yi-Zhao Zhang**[1], **Yu-Lu Liu**[1] and **Quan Zhou**[1],†

[1]Shanghai Key Laboratory of Mechanics in Energy Engineering, Shanghai Institute of Applied Mathematics and Mechanics, School of Mechanics and Engineering Science, Shanghai University, Shanghai 200072, PR China

(Received 21 May 2021; revised 5 November 2021; accepted 7 December 2021)

External modulation on thermal convection has been studied extensively to achieve the control of flow structures and heat-transfer efficiency. In this paper, we carry out direct numerical simulations on Rayleigh–Bénard convection accounting for both the modulation of wall shear and roughness over the Rayleigh number range $1.0 \times 10^6 \leq Ra \leq 1.0 \times 10^8$, the wall shear Reynolds number range $0 \leq Re_w \leq 5000$, the aspect-ratio range $2 \leq \Gamma \leq 4\pi$, and the dimensionless roughness height range $0 \leq h \leq 0.2$ at fixed Prandtl number $Pr = 1$. Under the combined actions of wall shear and roughness, with increasing Re_w, the heat flux is initially enhanced in the buoyancy-dominant regime, then has an abrupt transition near the critical shear Reynolds number $Re_{w,cr}$, and finally enters the purely diffusion regime dominated by shear. Based on the crossover of the kinetic energy production between the buoyancy-dominant and shear-dominant regimes, a physical model is proposed to predict the transitional scaling behaviour between $Re_{w,cr}$ and Ra, i.e. $Re_{w,cr} \sim Ra^{9/14}$, which agrees well with our numerical results. The reason for the observed heat-transport enhancement in the buoyancy-dominant regime is further explained by the fact that the moving rough plates introduce an external shear to strengthen the large-scale circulation (LSC) in the vertical direction and serve as a conveyor belt to increase the chances of the interaction between the LSC and secondary flows within cavities, which triggers more thermal plumes, efficiently transports the trapped hot (cold) fluids outside cavities.

Key words: Bénard convection, turbulent convection

† Email addresses for correspondence: jianzhao_wu@shu.edu.cn, qzhou@shu.edu.cn

1. Introduction

Thermal convection is ubiquitous in nature and industrial applications, such as lithospheric, oceanic and atmospheric circulations, and convective flows in heat exchangers or in pipes of power plants. The idealized model for studying thermal convection is Rayleigh–Bénard (RB) convection, i.e. a horizontal working fluid layer heated from below and cooled from above, which has been studied extensively over the past decades (Ahlers, Grossmann & Lohse 2009; Lohse & Xia 2010; Chillà & Schumacher 2012). According to the physical picture of an RB system, the convective heat transport is mainly characterized by the multi-scale interactions between the large-scale circulation (LSC) and thermal plumes detached from the boundary layers (BLs) (Grossmann & Lohse 2000). However, in most real-life situations, thermal convection can be much more complicated with the external shear and roughness, both of which affect the characteristics of the LSC and BLs. For instance, in the atmospheric circulation, the topology roughness and the horizontal wind both play an important role in the formation of thermoconvective storms (Bluestein 2013).

The introduction of roughness to RB convection has been proven to effectively break turbulent structures within BLs and significantly affect the heat-transport efficiency (Tisserand *et al.* 2011; Jiang *et al.* 2018; Dong *et al.* 2020). The first experiment on turbulent RB convection over pyramid-type rough elements by Shen, Tong & Xia (1996) and Du & Tong (1998) showed that wall roughness promotes the detachment of thermal plumes from the tip of roughness and thus enhances the heat transport. It is found that roughness-facilitated heat-transport enhancement exhibits not only an increase on the heat-transport scaling prefactor (Shen *et al.* 1996; Du & Tong 2000; Shishkina & Wagner 2011) but also an increase on the scaling exponent (Roche *et al.* 2001; Wei *et al.* 2014; Wagner & Shishkina 2015; Xie & Xia 2017). Xie & Xia (2017), Rusaouën *et al.* (2018) and Tummers & Steunebrink (2019) observed that roughness achieves the change on the heat-transport scaling exponent when the roughness height crosses over the thickness of thermal or viscous BLs. MacDonald *et al.* (2019) and Zhu *et al.* (2017, 2019) further pointed out that the $1/2$ scaling exponent achieved by roughness cannot be explained as the achievement of the ultimate regime, as the classical $1/3$ scaling can be recovered with the further increasing Rayleigh number (Ra). On the other hand, Zhang *et al.* (2018) revealed that roughness can also reduce the heat flux in some cases where the hot/cold fluids are trapped within the cavities. More recently, Yang *et al.* (2021) extended the observation to a much wider range of Prandtl numbers (Pr). Furthermore, Abtahi & Floryan (2017) and Hossain & Floryan (2020) showed that roughness can achieve the thermal drift and the pressure loss in RB convection.

The addition of shear induced by the mean flow (wind) in RB convection is expected to effectively affect the large-scale coherent structures, and thus causes significant changes on heat transport. Early experiments conducted by Solomon & Gollub (1990) showed the appearance of large-scale structures in sheared thermal convection, which is also numerically identified by Pirozzoli *et al.* (2017). By introducing the Couette-type shear into RB convection, Domaradzki & Metcalfe (1988) found that the heat transport is initially enhanced for low Ra, but is suppressed for $Ra \gtrsim 1.5 \times 10^5$ because the imposed shear breaks up the large-scale structures. Scagliarini, Gylfason & Toschi (2014) further carried out a numerical study of RB convection with the addition of the Poiseuille-type shear over $8.125 \times 10^5 \leq Ra \leq 1.3 \times 10^7$. It is also shown that the heat flux is initially reduced – since the structures of thermal plumes are swept away by the external shear – but then is enhanced when the shear dominates the convective flow and large-scale meandering streaks are formed. This finding was also observed in recent studies of wall-sheared RB

convection by Blass *et al.* (2020). Moreover, they proposed the Monin–Obukhov length to distinguish three different flow regimes in wall-sheared thermal convection, namely, buoyancy-dominant, transitional and shear-dominant regimes. A similar result was also found in the case of sheared stably stratified turbulence (Zonta & Soldati 2018). The effects of Pr on wall-sheared RB convection (Blass *et al.* 2021) and on sheared stably stratified flow (Langham, Eaves & Kerswell 2020) were further studied. Moreover, Scagliarini *et al.* (2015) studied the BL characteristics of sheared RB turbulence. Vishnu & Sameen (2020) investigated the influence of rotation-induced shear on the heat-transport scaling.

Although the pure influence of wall roughness or external shear has been studied extensively before, the combined effects of both are rarely explored. Hence, in this paper, we want to fill this gap and consider turbulent RB convection with both wall roughness and wall shear effects, focusing mainly on the flow structures and heat transport.

The remainder of this paper is organized as follows. Section 2 gives a brief description of the physical model and numerical method. The results of the shear-induced modulation on flow structures and heat transport are presented in § 3.1. In § 3.2, we give an explanation on shear-induced heat-transport enhancement in the buoyancy-dominant regime. In § 3.3, the influence of aspect ratio is discussed. In § 3.4, the influence of roughness height is studied. In § 3.5, a physical model is proposed to understand the transitional scaling based on the crossover of the total kinetic energy production between the buoyancy-dominant and shear-dominant regimes. Finally, a conclusion is presented in § 4.

2. Direct numerical simulation

We carry out direct numerical simulations (DNS) of wall-sheared RB convection over sinusoidally rough conducting plates in a two-dimensional rectangular cell, as shown in figure 1. The dimensionless governing equations for a sheared RB system are

$$\boldsymbol{\nabla}\cdot\boldsymbol{u}=0, \tag{2.1}$$

$$\partial_t\boldsymbol{u}+(\boldsymbol{u}\cdot\boldsymbol{\nabla})\boldsymbol{u}=-\boldsymbol{\nabla}p+(Ra/Pr)^{-1/2}\,\boldsymbol{\nabla}^2\boldsymbol{u}+\theta\boldsymbol{e}_z, \tag{2.2}$$

$$\partial_t\theta+(\boldsymbol{u}\cdot\boldsymbol{\nabla})\theta=(Ra\,Pr)^{-1/2}\,\boldsymbol{\nabla}^2\theta, \tag{2.3}$$

where t denotes the time non-dimensionalized by the free-fall time $\sqrt{H/(\alpha g\Delta)}$, $\boldsymbol{u}$ the velocity field normalized by the free-fall velocity $\sqrt{\alpha g\Delta H}$, θ the temperature scaled by the temperature difference Δ across the fluid layer, p the dimensionless kinematic pressure field, and $\boldsymbol{e}_z$ the unit vector along the vertical direction, respectively. The external shear is introduced by moving the top and bottom plates in opposite directions with a dimensionless velocity u_w as depicted in figure 1. For the sheared RB convection with roughness, there are six control parameters: the Rayleigh number $Ra=\alpha g\Delta H^3/(\nu\kappa)$, the Prandtl number $Pr=\nu/\kappa$, the aspect ratio $\Gamma=L/H$, the dimensionless roughness height h, the dimensionless roughness wavelength λ, and the shear Reynolds number $Re_w=\sqrt{Ra/Pr}\,u_w$, where g is the gravitation magnitude, α, ν and κ are respectively the volumetric coefficient of thermal expansion, the kinematic viscosity and the thermal diffusivity of the working fluid, and H and L denote respectively the dimensional height and width of the RB cell.

In all simulations, we fix the Prandtl number $Pr=1$. As all length scales are normalized by H, we take the dimensionless roughness wavelength $\lambda=0.2$ for all runs. Note that the cell height H is defined between both mean surfaces of rough plates as depicted in figure 1, which guarantees that the rough cell has the same fluid volume as the

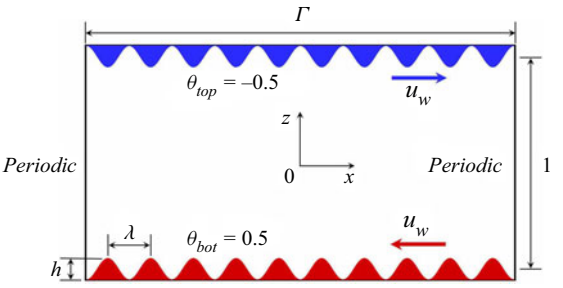

Figure 1. Sketch of wall-sheared Rayleigh–Bénard convection over rough surfaces with the coordinate system. Sinusoidal roughness elements of the dimensionless height h and wavelength λ are located on both plates, which move in opposite directions with horizontal velocities $\pm u_w$.

smooth cases (Zhu *et al.* 2017). The Rayleigh number Ra varies from 10^6 to 10^8, the shear Reynolds number Re_w from 0 to 5000, the aspect ratio from $\Gamma = 2$ to $\Gamma = 4\pi$, and the dimensionless roughness height from $h = 0$ to $h = 0.2$. All simulations are performed using a fourth-order finite-difference code (Zhang *et al.* 2018, 2019) with staggered grids. No-slip boundary conditions are applied for the velocity fields, constant temperatures $\theta_{bot} = 0.5$ and $\theta_{top} = -0.5$ for the bottom and top plates, respectively, and periodic boundary conditions are adopted in the horizontal direction. An immersed boundary method is used to track the moving rough walls (Fadlun *et al.* 2000). The grid resolution depends on both Ra and Re_w, and non-equidistant meshes are implemented in the vertical direction, which are refined close to both solid surfaces to fully resolve the rough boundaries. Figures 2(*a*) and 2(*b*) show the horizontal and vertical resolutions that we used in numerical simulations of $\Gamma = 2$ and $h = 0.1$, respectively. Figures 2(*c* and 2*d*) give an example for $Ra = 10^8$, $Re_w = 5000$, $\Gamma = 2$ and $h = 0.1$ to show that our simulations are fully resolved for the chosen resolutions. The details for numerical parameters and results for all runs are given in Appendix A.

3. Results and discussion

3.1. *Shear-induced modulation*

We first quantitatively study the modulated effects of wall shear on heat-transport efficiency in RB convection over rough surfaces at $\Gamma = 2$ and $h = 0.1$. The dimensionless global heat flux is measured by the Nusselt number $Nu = \sqrt{Ra\,Pr}\langle w\theta\rangle_{t,s} - \langle\partial_z\theta\rangle_{t,s}$, where w is the vertical component of velocity and $\langle\cdot\rangle_{t,s}$ indicates an average over time and the mid-height horizontal section. All statistics in the present study are calculated over more than 600 free-fall time units after the convective flow has reached the statistically steady state.

Figure 3(*a*) depicts the measured Nu depending on the modulation shear Reynolds number Re_w. It is shown that the Re_w-dependence of Nu exhibits some kind of similar trends for different Ra, i.e. there exists a critical shear Reynolds number $Re_{w,cr}$ depending on Ra. A significant heat-transport enhancement regime induced by wall shear is observed below $Re_{w,cr}$. On the other hand, above $Re_{w,cr}$, a purely diffusion regime is reached and Nu takes the minimum value. Between these two regimes, Nu decreases sharply and an abrupt transition occurs. To show the enhancement effects, we plot in figure 3(*b*) the measured Nu normalized by the corresponding value of $Nu(0)$ at $Re_w = 0$. It is seen that $Nu/Nu(0)$ increases initially with increasing Ra with a maximal enhancement of $\sim$76 %

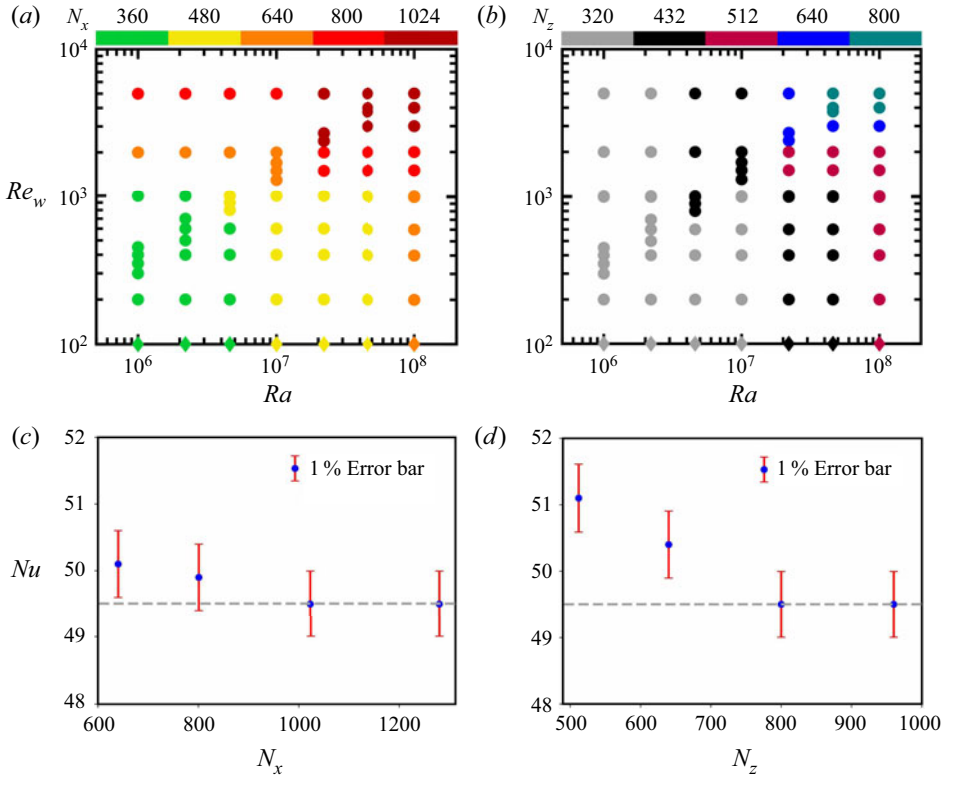

Figure 2. Horizontal grid number N_x (a) and vertical grid number N_z (b) of the first part of numerical simulations at $\Gamma = 2$ and $h = 0.1$ (rhombus points for the cases at $Re_w = 0$). Values of the Nusselt number Nu for simulations at $Ra = 1.0 \times 10^8$ and $Re_w = 5000$ performed using different N_x at fixed $N_z = 800$ (c) and different N_z at fixed $N_x = 1024$ (d). The dashed lines indicate the chosen value.

at $Ra = 1.0 \times 10^8$. Such a high Nu-enhancement is really non-trivial, implying that the shear-induced modulation on turbulent RB convection over rough plates exhibits some features that are different from the smooth cases (Scagliarini *et al.* 2014; Blass *et al.* 2020), in which Nu initially decreases with Re_w. Note that Wagner & Shishkina (2015) found an upper bound of heat-transfer enhancement purely by regular surface roughness, i.e. $Nu/Nu_s(0) \leq A_w/A_s$, where $Nu_s(0)$ is the Nusselt number of smooth cases without shear, A_w is the wetted covering surface area over roughness, and A_s is the covering area over smooth surface. However, it is found in our study that the maximal enhancement rate $Nu/Nu_s(0) \approx 1.94$ at $Ra = 10^8$ and $Re_w = 5000$ exceeds the upper bound $A_w/A_s \approx 1.46$ under the effect of external shear.

We next examine the shear-induced modulation on the strength of the large-scale flow, which is characterized by the Reynolds number $Re_z = \sqrt{Ra/Pr}\, W$. Here, $W = \sqrt{\langle w^2 \rangle_{t,v}}$ is the root-mean-square (r.m.s.) vertical velocity, and $\langle \cdot \rangle_{t,v}$ denotes an average over time and the whole volume. Figure 4 shows the calculated Re_z as a function of Re_w at various Ra, and a sharp transition is also observed around $Re_{w,cr}$. When comparing figures 3 and 4, it is clearly seen that the strongest (weakest) strength of the LSC corresponds to the maximal (minimal) heat transport, suggesting that the imposed wall shear may modulate the convective heat transport via changing the flow structures in rough cells.

To gain more insight into this modulation, we analyse how flow structures are changed under the imposition of wall shear. Figure 5 shows the instantaneous temperature fields

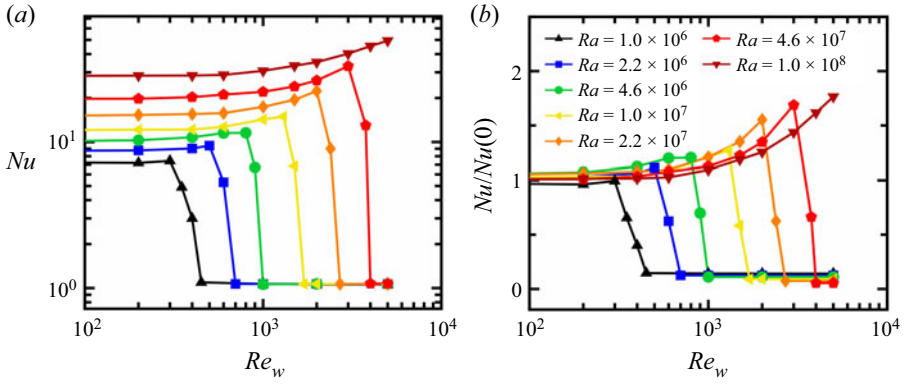

Figure 3. Shear-induced modulation on the heat transport in RB convection over rough plates at $\Gamma = 2$ and $h = 0.1$. The measured Nu (a) and $Nu/Nu(0)$ (b) are functions of Re_w at different Ra. Here, $Nu(0)$ is the value of Nu measured at $Re_w = 0$.

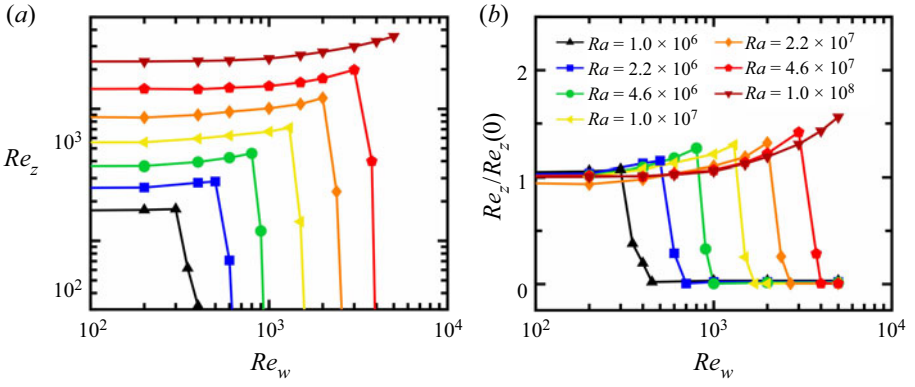

Figure 4. Shear-induced modulation on the magnitude of the LSC in the vertical direction at $\Gamma = 2$ and $h = 0.1$. The measured Re_z (a) and $Re_z/Re_z(0)$ (b) are functions of Re_w at different Ra. Here, $Re_z(0)$ is the value of Re_z measured at $Re_w = 0$.

overlaid by the velocity fields at $Ra = 1.0 \times 10^7$ for three different Re_w. When the wall shear effect is small (see figure 5a), the dominant flow consists of two large-scale rolls (LSRs) that are similar to those in standard RB convection. We note that the sizes of the two rolls are not equal; the one (clockwise) whose velocity near the plates is in the same direction as the corresponding moving plate expands horizontally, and the other one (anticlockwise) shrinks. With increasing Re_w, the expanded clockwise large-scale roll gets wider. At $Re_{w,cr}$ in the transitional regime, the width of the clockwise roll exceeds the cell's length and thus the larger roll covers the whole fluid volume as shown in figure 5(b). With a further increase in Re_w, the flow is then dominated by wall shear and laminar Couette flow for the velocity field, and heat conduction for the temperature field can be identified as depicted in figure 5(c). This suggests that the modulation effect is determined by the competition between the wall shear and the buoyancy.

Figure 6(a) then shows the phase diagram of different regimes in the Re_w, Ra plane in cases $\Gamma = 2$ and $h = 0.1$: the buoyancy-dominant regime, the transitional regime and the shear-dominant regime. One can see that Re_w–Ra for the transitional regime exhibits a linear relation in a log-log coordinate, indicating that there exists a transitional scaling

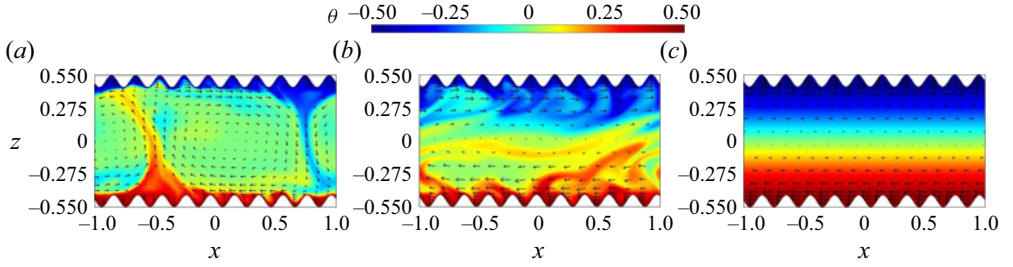

Figure 5. Typical snapshots of the instantaneous temperature (colour) and velocity (arrows) fields at $Ra = 1.0 \times 10^7$, $\Gamma = 2$ and $h = 0.1$ for three different Re_w: (*a*) $Re_w = 600$ in the buoyancy-dominant regime, (*b*) $Re_w = 1500$ in the transitional regime and (*c*) $Re_w = 1700$ in the shear-dominant regime. The corresponding movies are provided in the supplementary movies available at https://doi.org/10.1017/jfm.2021.1111.

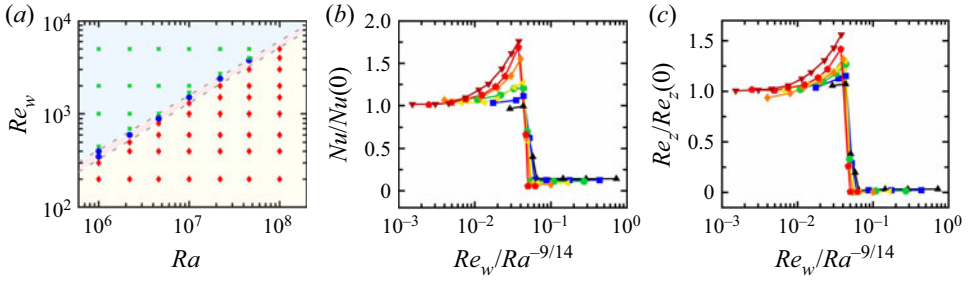

Figure 6. (*a*) Explored phase diagram of different regimes in the Re_w, Ra plane for $\Gamma = 2$ and $h = 0.1$. The dashed lines (grey) are the eye-guided borders in between the three regimes: the buoyancy-dominant regime (regime I, coloured light yellow), the transitional regime (regime II, coloured light pink) and the shear-dominant regime (regime III, coloured light cyan). Here, red diamond points refer to the cases in regime I, blue solid dots refer to the cases in regime II, and green crosses refer to the cases in regime III. (*b*,*c*) Normalized $Nu/Nu(0)$ (*b*) and $Re_z/Re_z(0)$ (*c*) as functions of $Re_w Ra^{-9/14}$. The symbols in (*b*,*c*) are the same as those in figures 3 and 4.

relation between the critical shear Reynolds number $Re_{w,cr}$ and the Rayleigh number Ra. With the transitional scaling $Re_{w,cr} \sim Ra^{9/14}$ predicted by a physical model in § 3.5, we replot in figures 6(*b*) and 6(*c*) the normalized $Nu/Nu(0)$ of figure 3(*b*) and the normalized $Re_z/Re_z(0)$ of figure 4(*b*) vs the rescaled $Re_w Ra^{-9/14}$ for various Ra. Now all data points in the transitional regime roughly collapse on top of each other, indicating that the predicted scaling $Re_{w,cr} \sim Ra^{9/14}$ can well describe the transition behaviour.

3.2. *Heat-transport enhancement in the buoyancy-dominant regime*

As discussed above, *Nu*-enhancement is observed in the buoyancy-dominant regime (see figure 6*b*). This finding is different from *Nu* being initially suppressed by the shear-induced plume-sweeping effects in previous studies of Couette–RB (Blass *et al.* 2020, 2021) or Poiseuille–RB (Scagliarini *et al.* 2014) convection over smooth plates. Then the question is how the heat-transfer efficiency is improved in rough cases.

We begin by looking at the instantaneous flow structures in the buoyancy-dominant regime at $Ra = 1.0 \times 10^8$, $\Gamma = 2$ and $h = 0.1$ as shown in figure 7. The moving rough plates serve as conveyor belts and provide the equivalent occurrence of the interaction between the LSC and the secondary flow in each cavity. This efficiently pumps the trapped hot (cold) fluids outside the cavities. These pumped hot (cold) fluids then enter the bulk,

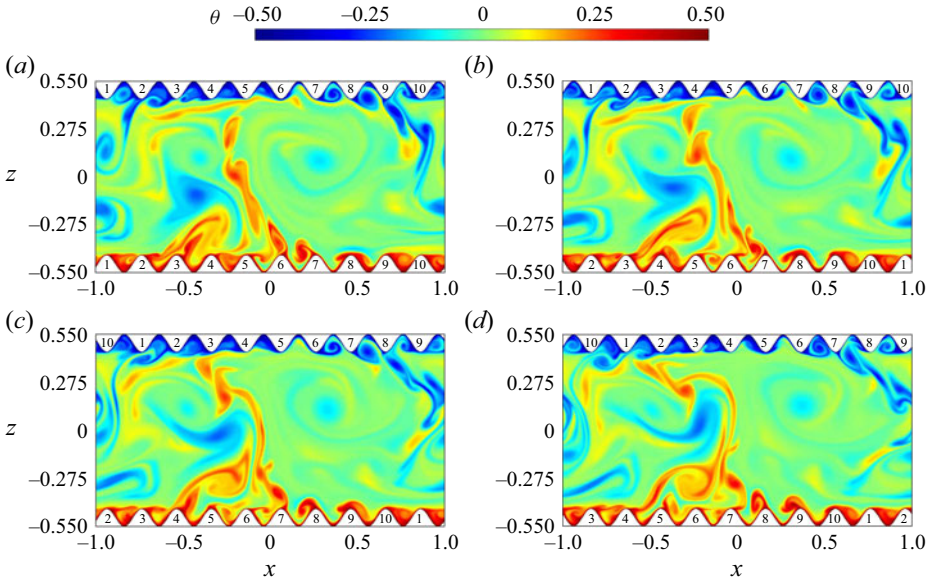

Figure 7. Snapshots of the temperature fields in the buoyancy-dominant regime of sheared RB convection over moving rough plates at $Ra = 1.0 \times 10^8$, $\Gamma = 2$, $h = 0.1$ and $Re_w = 5000$. (*a*,*b*) The LSC interacts with the secondary flow inside the cavity between rough elements 6 and 7. The trapped hot fluid is sloshed out and transported to the bulk from $t = 1812.0$ to $t = 1812.2$. (*c*,*d*) The same process is repeated at the cavity between rough elements 7 and 8 from $t = 1812.4$ to $t = 1812.6$. The complete process is shown by the movie in the supplementary movies.

group and merge together, and strengthen the vertical motion of the LSC (see figure 4). Figure 7 shows an example of this process at four consecutive instants. At $t = 1812.0$ (figure 7*a*), the LSC starts to interact with the secondary flow in the cavity between rough elements 6 and 7, and the trapped hot fluid is then sloshed to the bulk at $t = 1812.2$ (figure 7*b*), which transports the accumulated heat from the cavity into the bulk. As time goes on, the same interaction is repeated between the LSC and the secondary flow in the cavity between roughness 7 and 8 from $t = 1812.4$ (figure 7*c*) to $t = 1812.6$ (figure 7*d*).

We notice that for the present parameter ranges the global heat transport is dominated mainly by thermal BLs, as the convective flow is still in the so-called 'classical' regime. This prompts us to investigate directly the spatial distribution of thermal BL thickness $\delta_{th}(x)$. Figure 8 shows $\delta_{th}(x)$ near the bottom plates for various Re_w in the buoyancy-dominant regime, where δ_{th} is evaluated by the 'slope' method (Zhou & Xia 2013), i.e. the vertical position at which the tangent line of the time-averaged temperature profiles perpendicular to roughness within the thermal BL coincides with the mean bulk temperature. It is clearly observed that with increasing Re_w, the modulation of wall shear increases the emissions of trapped hot fluids from the cavities, which significantly leads to a decrease on $\delta_{th}(x)$. The reduction of $\delta_{th}(x)$ as shown in figure 8 further suggests that the moving rough plates promote the interactions between the LSC and secondary flows within each cavity and thus stimulate the ejection of thermal plumes from thermal BLs and enhance heat transport.

To further examine this mechanism, we extract thermal plumes from the instantaneous fields and collect their heat content Q_p, area A_p and vorticity Ω_p as shown in figure 9. The criteria for identifying plumes are given by $|\theta - \langle\theta\rangle_{t,s}| > \theta_{rms}$ and $\sqrt{Ra\,Pr}\,w\theta > Nu$ (Huang *et al.* 2013; van der Poel *et al.* 2015; Wang, Zhou & Sun 2020), where

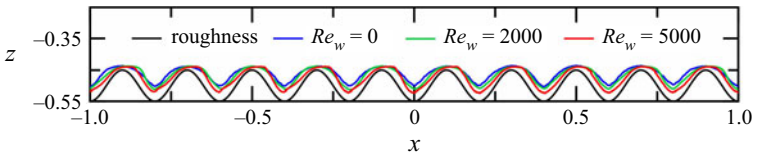

Figure 8. Horizontal distribution of time-averaged thermal BL thickness $\delta_{th}(x)$ near the bottom plate at $Ra = 1.0 \times 10^8$, $\Gamma = 2$ and $h = 0.1$ for various Re_w in the buoyancy-dominant regime. Overall, δ_{th} decreases with growing Re_w.

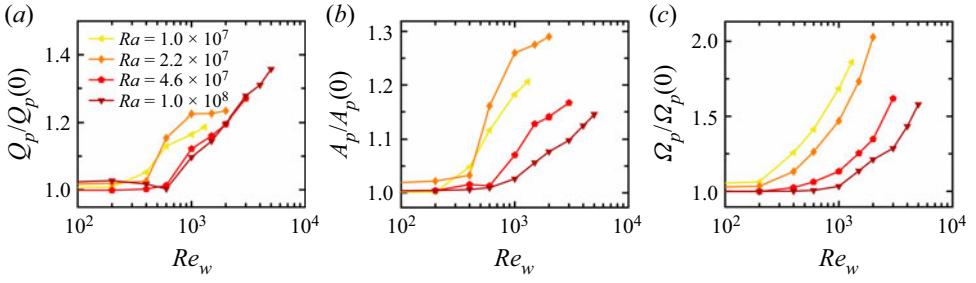

Figure 9. Normalized heat content $Q_p/Q_p(0)$ (a), area $A_p/A_p(0)$ (b) and vorticity $\Omega_p/\Omega_p(0)$ (c) of extracted thermal plumes as functions of Re_w at $\Gamma = 2$ and $h = 0.1$ for different Ra.

$\theta_{rms} = \sqrt{\langle\theta^2\rangle_{t,s} - \langle\theta\rangle_{t,s}^2}$ is the r.m.s. temperature. We calculate the plume area as $A_p = \sum V_{grid}$, the heat content as $Q_p = \sum V_{grid}\theta$, and the vorticity contained in the plumes as $\Omega_p = \sum V_{grid}(\partial_x w - \partial_z u)$, where V_{grid} is the volume of each grid point. Only the hot plumes are used for calculating those statistics. As depicted in figure 9(a,b), both the area and heat content of hot plumes increase with Re_w for large Re_w at different Ra. For instance, at the highest Re_w studied for $Ra = 10^8$, the heat content and area rise by 35.7 % and 14.6 %, respectively. Moreover, figure 9(c) shows that the vorticity within plumes is enhanced by wall shear for different Ra, implying that the small eddies inside plumes produce a stronger mixing at high Re_w in the buoyancy-dominant regime. Taken together, these results confirm quantitatively that with increasing Re_w, the wall shear strengthens the LSC and the vorticity within plumes, leading to an intense heat mixing; the moving plates increase the chances of interactions between the LSC and secondary flows within each cavity, which triggers more plume emissions and thins thermal BLs. This gives rise to a significant heat-transport enhancement in the buoyancy-dominant regime of sheared RB convection over rough plates.

3.3. *The influence of aspect ratio*

Next, we are interested in the shear-induced modulation on thermal convection with multiple-rolls structures and examine whether the transition from the buoyancy-dominant regime to the shear-dominant regime still occurs in cases of large aspect ratios.

Figure 10 shows the measured Nu as a function of Re_w with various Ra at large aspect ratios $\Gamma = 2\pi$ and $\Gamma = 4\pi$. It is clearly seen for large aspect-ratio cases that the action of shear still achieves the sharp transition from the buoyancy-dominant regime to the shear-dominant regime, which leads to an abrupt reduction of Nu. This observation is consistent with the results of $\Gamma = 2$ as shown in figure 3. Taken together, it is demonstrated that the occurrence of the transition is due to the shear-induced modifications on convective flows rather than the limitation of cell length.

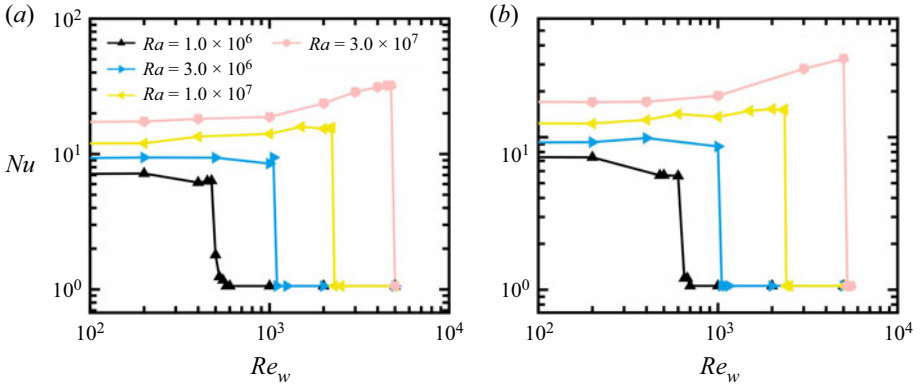

Figure 10. Shear-induced modification on the heat transport Nu in convection cells with different aspect ratios Γ. The measured Nu are functions of Re_w at $\Gamma = 2\pi$ (a), $\Gamma = 4\pi$ (b) and fixed $h = 0.1$. Here, the cyan and pink lines represent the statistics of additional $Ra = 3.0 \times 10^6$ and $Ra = 3.0 \times 10^7$, and other lines keep the same Ra values as those in figure 3.

Taking a closer look at figure 10, it is found that the trend of Nu in the buoyancy-dominant regime at larger Γ becomes more flexural with growing Re_w, compared to that at $\Gamma = 2$. It is seen that Nu is enhanced initially both at $\Gamma = 2\pi$ and $\Gamma = 4\pi$ at high Ra, which is caused by combined effects of wall shear and roughness as discussed in § 3.2. This suggests that this mechanism of heat-transport enhancement still plays an important role in RB convection with multiple rolls. However, it is also seen that Nu is slightly reduced at low Ra for $\Gamma = 2\pi$ and $\Gamma = 4\pi$. This is probably because at low Ra, thermal convection is not plume-dominant, the proposed heat transport enhancement mechanism does not work, and the convective flow is mainly laminar; shear-induced stratification of the velocity field reduces the vertical velocity, and consequently suppresses convective heat transport.

We then examine the shear-induced modification on flow structures in the buoyancy-dominant regime for large Γ. Figure 11 shows the instantaneous flow structures at $h = 0.1$, $\Gamma = 2\pi$ and $Ra = 1.0 \times 10^7$ with different shear Reynolds numbers $Re_w = 0$, 1500, 2225. It is found that under the action of external shear, the multiple rolls begin to be expanded for the clockwise direction and be shrunk for the anticlockwise direction (see figure 11b), then the adjacent rolls merge until the flow structures with a clockwise roll of large size and an anticlockwise roll of small size (see figure 11c). This indicates that for cases of large Γ, the external shear initially reduces the number of LSRs until attaining two-roll structures as $\Gamma = 2$ in the buoyancy-dominant regime, then enters the shear-dominant regime through an abrupt transition.

Further, we examine the influence of the aspect ratio on the transitional scaling. Figure 12 shows the compensative phase diagram of flow regimes with various aspect ratios $\Gamma = 2, 2\pi, 4\pi$, where Re_w is rescaled by the proposed transitional scaling $Re_{w,cr} \sim Ra^{9/14}$ in § 3.5. It is found that the fitted transitional scalings at different Γ values are basically consistent with the scaling predicted by our proposed model in § 3.5, although the effect of the aspect ratio leads to a small discrepancy between the scaling exponents.

3.4. *The influence of roughness height*

In this subsection, we study wall-sheared RB convection with various roughness heights and figure out the influence of roughness on shear-induced modulation on heat transfer.

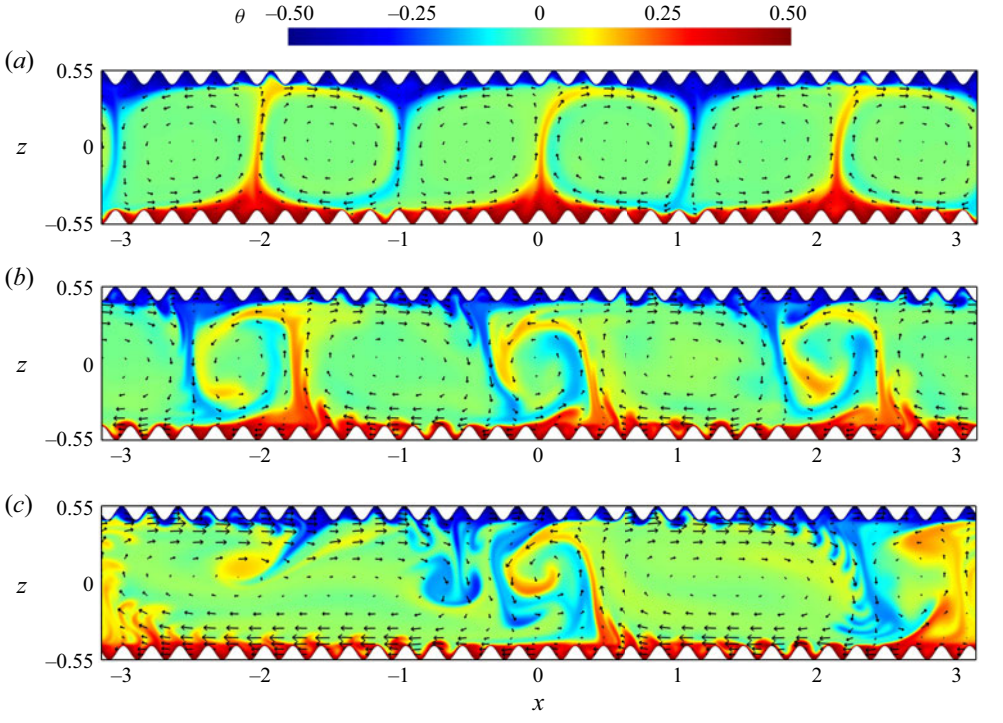

Figure 11. Typical snapshots of the instantaneous temperature (colour) and velocity (arrows) fields for three different Re_w in the buoyancy-dominant regime at $h = 0.1$, $\Gamma = 2\pi$ and $Ra = 1.0 \times 10^7$: (*a*) $Re_w = 0$, (*b*) $Re_w = 1500$ and (*c*) $Re_w = 2225$.

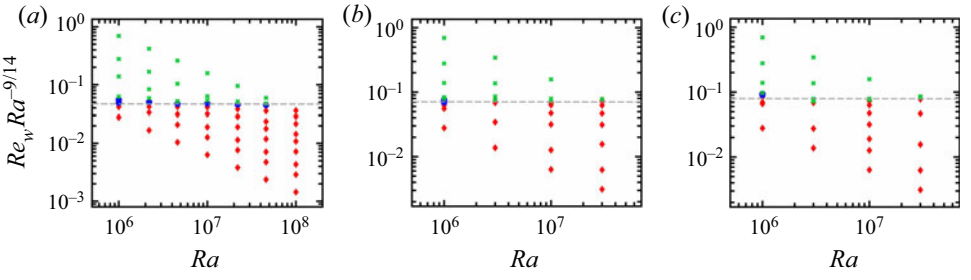

Figure 12. Compensative phase diagrams of flow regimes with different cell aspect ratios Γ. Panels (*a*), (*b*) and (*c*) are respectively the plots of convections at $\Gamma = 2$, $\Gamma = 2\pi$ and $\Gamma = 4\pi$, and fixed $h = 0.1$. Here, the symbols in all plots are the same as those in figure 6(*a*). The dashed line is drawn as a guide for the eye.

Figure 13 shows the measured Nu as a function of Re_w for different Ra with various roughness heights $h = 0$, $h = 0.05$ and $h = 0.2$ at fixed $\Gamma = 2$. For the smooth case ($h = 0$), it is seen that Nu is nearly unchanged in the buoyancy-dominated regime, then slowly transits to the minimum value in the shear-dominant regime. This result shows that shear-induced modification on heat transfer for two-dimensional cases is different from that for three-dimensional cases as studied by (Blass *et al.* 2020, 2021) in thermal convection over smooth surfaces, due to the lack of fluid motion in the third direction. When the roughness is applied, the mechanism of heat transfer enhancement due to the

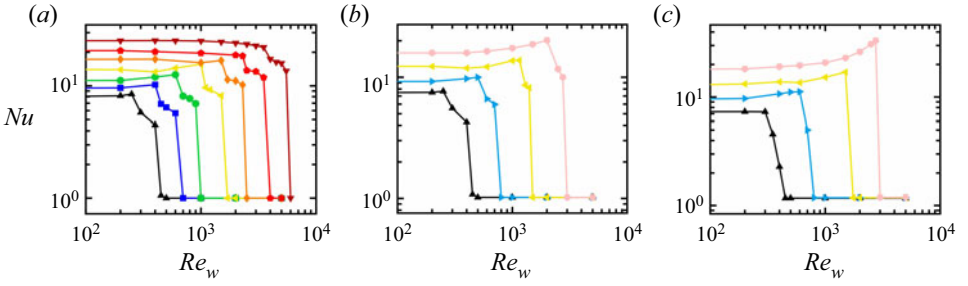

Figure 13. Shear-induced modification on the heat transport Nu in convection cells with different roughness heights h. The measured Nu are functions of Re_w at $h = 0$ (*a*), $h = 0.05$ (*b*), $h = 0.2$ (*c*), and fixed $\Gamma = 2$.

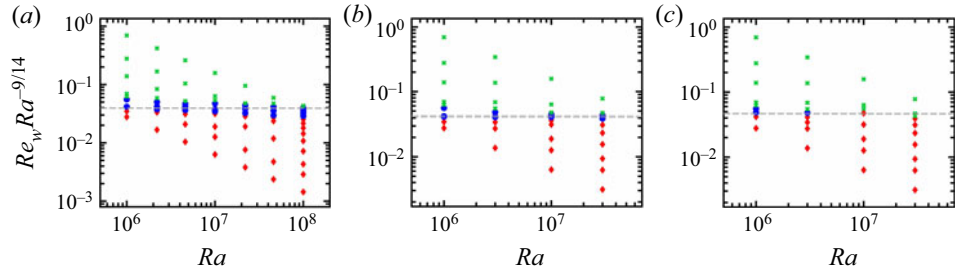

Figure 14. Compensative phase diagrams of flow regimes with different roughness heights h. Panels (*a*), (*b*) and (*c*) are respectively the plots of convections with $h = 0$, $h = 0.05$, $h = 0.2$, and fixed $\Gamma = 2$. Here, the symbols in all plots are the same as those in figure 6(*a*). The dashed line is drawn as a guide for the eye.

combined effects of roughness and shear begins to work, Nu tends to be enhanced, and with increasing h, the maximal Nu-enhancement rate becomes larger.

Next, we examine the roughness effect on the transitional scaling. Figure 14 depicts the phase diagrams of flow regimes of the wall-sheared RB convection at various roughness heights $h = 0, 0.05, 0.2$, where Re_w is rescaled by the proposed transitional scaling $Re_{w,cr} \sim Ra^{9/14}$ in § 3.5. It is observed that the transitional region narrows with increasing h but its location shows a weak dependency on h. It seems that the transitional scalings with different h are quite close to the predicted scaling in § 3.5, implying that the roughness height has only a slight influence on shear-induced modulation mechanism.

3.5. *Physical understanding of the transitional scaling*

As it is concluded in § 3.4 that the roughness height has only few influences on the transitional scaling, we take the smooth cases in the following for simplification. To better understand shear-induced modulation, we take advantage of the dynamic equation of global kinetic energy $E(t) = \frac{1}{2}\langle|\boldsymbol{u}|^2\rangle_v$ to obtain

$$\frac{\mathrm{d}E(t)}{\mathrm{d}t} = P_{buo}(t) + P_{shear}(t) - \epsilon(t), \tag{3.1}$$

where $P_{buo} = \langle w\theta\rangle_v$ denotes the buoyancy-induced production, $P_{shear} = \frac{1}{2}\langle\nabla^2|\boldsymbol{u}|^2\rangle_v/\sqrt{Ra/Pr}$ means the wall-shear-induced production, $\epsilon = \langle|\nabla\boldsymbol{u}|^2\rangle_v/\sqrt{Ra/Pr}$ is the dissipation rate, and $|\cdot|$ denotes the vector or tensor norm. In (3.1), the competition mechanism can be quantified by the productions for the kinetic energy by the shear and

No.	Ra	Re_w	Γ	h	N_x	N_z	δt	Nu	Re_z
1	1.0×10^6	0	2	0	360	256	1.0×10^{-3}	7.58	204.5
2	1.0×10^6	200	2	0	360	256	1.0×10^{-4}	8.15	211.7
3	1.0×10^6	250	2	0	360	256	1.0×10^{-4}	8.44	212.5
4	1.0×10^6	300	2	0	360	256	5.0×10^{-5}	5.78	87.0
5	1.0×10^6	400	2	0	360	256	2.0×10^{-5}	4.50	57.5
6	1.0×10^6	450	2	0	360	256	2.0×10^{-5}	1.05	4.1
7	1.0×10^6	500	2	0	360	256	2.0×10^{-5}	1.00	0.0
8	1.0×10^6	1000	2	0	360	256	1.0×10^{-5}	1.00	0.0
9	1.0×10^6	2000	2	0	640	256	1.0×10^{-5}	1.00	0.0
10	1.0×10^6	5000	2	0	800	256	1.0×10^{-5}	1.00	0.0
11	2.2×10^6	0	2	0	360	256	5.0×10^{-4}	9.28	315.8
12	2.2×10^6	200	2	0	360	256	1.0×10^{-4}	9.60	318.5
13	2.2×10^6	400	2	0	360	256	5.0×10^{-5}	10.3	330.0
14	2.2×10^6	450	2	0	360	256	2.0×10^{-5}	6.87	130.0
15	2.2×10^6	500	2	0	360	256	2.0×10^{-5}	6.42	115.5
16	2.2×10^6	600	2	0	360	256	2.0×10^{-5}	5.77	92.0
17	2.2×10^6	1000	2	0	360	256	1.0×10^{-5}	1.00	0.0
18	2.2×10^6	2000	2	0	640	256	1.0×10^{-5}	1.00	0.0
19	2.2×10^6	5000	2	0	800	256	1.0×10^{-5}	1.00	0.0
20	4.6×10^6	0	2	0	360	256	5.0×10^{-4}	11.1	469.6
21	4.6×10^6	200	2	0	360	256	1.0×10^{-4}	11.2	470.3
22	4.6×10^6	400	2	0	360	256	5.0×10^{-5}	12.0	481.0
23	4.6×10^6	600	2	0	360	256	5.0×10^{-5}	12.6	494.1
24	4.6×10^6	700	2	0	480	256	2.0×10^{-5}	8.10	193.0
25	4.6×10^6	800	2	0	480	256	2.0×10^{-5}	7.70	170.0
26	4.6×10^6	900	2	0	480	256	2.0×10^{-5}	6.94	139.0
27	4.6×10^6	1000	2	0	480	256	2.0×10^{-5}	1.00	0.0
28	4.6×10^6	2000	2	0	640	256	1.0×10^{-5}	1.00	0.0
29	4.6×10^6	5000	2	0	800	256	1.0×10^{-5}	1.00	0.0
30	1.0×10^7	0	2	0	360	256	2.0×10^{-4}	14.2	693.3
31	1.0×10^7	200	2	0	360	256	1.0×10^{-4}	14.0	710.2
32	1.0×10^7	400	2	0	360	256	1.0×10^{-4}	13.3	723.5
33	1.0×10^7	600	2	0	360	256	5.0×10^{-5}	14.4	726.0
34	1.0×10^7	1000	2	0	480	256	2.0×10^{-5}	15.6	760.0
35	1.0×10^7	1100	2	0	480	256	2.0×10^{-5}	9.64	300.1
36	1.0×10^7	1200	2	0	480	256	2.0×10^{-5}	9.25	265.0
37	1.0×10^7	1500	2	0	480	256	2.0×10^{-5}	8.18	200.5
38	1.0×10^7	1700	2	0	480	256	2.0×10^{-5}	1.00	0.0
39	1.0×10^7	2000	2	0	640	256	1.0×10^{-5}	1.00	0.0
40	1.0×10^7	5000	2	0	800	256	1.0×10^{-5}	1.00	0.0
41	2.2×10^7	0	2	0	480	320	2.0×10^{-4}	17.2	1075
42	2.2×10^7	200	2	0	480	320	1.0×10^{-4}	17.3	1067
43	2.2×10^7	400	2	0	480	320	1.0×10^{-4}	17.3	1061
44	2.2×10^7	1000	2	0	480	320	5.0×10^{-5}	16.1	1145
45	2.2×10^7	1500	2	0	480	320	2.0×10^{-5}	16.9	1189
46	2.2×10^7	1700	2	0	640	320	2.0×10^{-5}	11.4	439.0
47	2.2×10^7	2000	2	0	640	320	2.0×10^{-5}	11.1	394.2
48	2.2×10^7	2300	2	0	640	320	2.0×10^{-5}	10.2	331.0
49	2.2×10^7	2500	2	0	640	320	1.0×10^{-5}	1.00	0.0
50	2.2×10^7	5000	2	0	800	320	1.0×10^{-5}	1.00	0.0

Table 1. For caption see next page.

No.	Ra	Re_w	Γ	h	N_x	N_z	δt	Nu	Re_z
51	4.6×10^7	0	2	0	480	320	2.0×10^{-4}	20.8	1577
52	4.6×10^7	200	2	0	480	320	2.0×10^{-4}	20.7	1584
53	4.6×10^7	400	2	0	480	320	1.0×10^{-5}	20.3	1637
54	4.6×10^7	1000	2	0	480	320	5.0×10^{-5}	19.7	1676
55	4.6×10^7	2000	2	0	640	320	2.0×10^{-5}	18.9	1718
56	4.6×10^7	2300	2	0	640	320	2.0×10^{-5}	18.5	1690
57	4.6×10^7	2500	2	0	640	320	1.0×10^{-5}	13.7	654.0
58	4.6×10^7	3000	2	0	640	320	1.0×10^{-5}	13.4	584.0
59	4.6×10^7	3500	2	0	640	320	1.0×10^{-5}	11.9	481.0
60	4.6×10^7	4000	2	0	800	320	1.0×10^{-5}	1.00	0.0
61	4.6×10^7	5000	2	0	800	320	1.0×10^{-5}	1.00	0.0
62	1.0×10^8	0	2	0	640	320	1.0×10^{-4}	25.5	2417
63	1.0×10^8	200	2	0	640	320	1.0×10^{-4}	25.4	2418
64	1.0×10^8	400	2	0	640	320	1.0×10^{-4}	25.5	2449
65	1.0×10^8	600	2	0	640	320	1.0×10^{-4}	25.4	2445
66	1.0×10^8	1000	2	0	640	320	8.0×10^{-5}	25.2	2508
67	1.0×10^8	1500	2	0	800	320	5.0×10^{-5}	24.8	2580
68	1.0×10^8	2000	2	0	800	320	2.0×10^{-5}	24.2	2599
69	1.0×10^8	2500	2	0	800	320	2.0×10^{-5}	23.6	2607
70	1.0×10^8	3000	2	0	800	320	1.0×10^{-5}	22.9	2605
71	1.0×10^8	3500	2	0	800	320	1.0×10^{-5}	22.2	2594
72	1.0×10^8	4000	2	0	800	320	1.0×10^{-5}	17.4	963.0
73	1.0×10^8	4500	2	0	800	320	1.0×10^{-5}	16.4	885.0
74	1.0×10^8	5000	2	0	800	320	1.0×10^{-5}	16.0	808.0
75	1.0×10^8	5500	2	0	800	320	1.0×10^{-5}	13.6	670.0
76	1.0×10^8	6000	2	0	800	320	1.0×10^{-5}	1.00	0.0

Table 1. Cases at $\Gamma = 2$ and $h = 0$.

the buoyancy. Depending on the relative importance of the time-averaged $\bar{P}_{buo} = \langle w\theta \rangle_{t,v}$ and $\bar{P}_{shear} = \frac{1}{2}\langle \nabla^2 |\boldsymbol{u}|^2 \rangle_{t,v} / \sqrt{Ra/Pr}$ in the total production $\bar{P} = \bar{P}_{buo} + \bar{P}_{shear}$ for the global kinetic energy, we can obtain the three regimes presented in figures 6, 12 and 14.

Regime I: the buoyancy-induced production $\bar{P}_{buo}$ is dominant, and flow structures resemble large-scale rolls as those found in standard RB convection. This is the buoyancy-dominant regime, in which a heat-transport enhancement is observed and the Nu-enhancement rate becomes larger with ascending Ra.

Regime II: there is a balance between the buoyancy-induced production $\bar{P}_{buo}$ and the shear-induced production $\bar{P}_{shear}$. Sharp transitions exist in figures 6, 10 and 13. In this regime, the LSC nearly disappears, the velocity field of flow tends to be stably stratified, and the temperature field tends to be in a pure diffusion state. Here, Nu decreases dramatically from maximum to minimum.

Regime III: the shear-induced production $\bar{P}_{shear}$ is dominant, and the wall shear effect is strong enough to dominate the flow. This is the shear-dominant regime, in which the flow is nearly laminar Couette flow and the global heat transport is determined mainly by thermal conduction.

According to the physical picture of different regimes, we can make the approximation of the total production $\bar{P}$, namely, $\bar{P} \sim \bar{P}_{buo}$ in the buoyancy-dominant regime and $\bar{P} \sim \bar{P}_{shear}$ in the shear-dominant regime. First, as the heat flux is the same in any

No.	Ra	Re_w	Γ	h	N_x	N_z	N_h	δt	Nu	Re_z
1	1.0×10^6	0	2	0.05	360	280	25	1.0×10^{-3}	7.31	185.3
2	1.0×10^6	200	2	0.05	360	280	25	1.0×10^{-4}	7.51	193.1
3	1.0×10^6	250	2	0.05	360	280	25	5.0×10^{-5}	7.67	195.0
4	1.0×10^6	300	2	0.05	360	280	25	2.0×10^{-5}	5.56	82.0
5	1.0×10^6	400	2	0.05	360	280	25	2.0×10^{-5}	4.26	53.0
6	1.0×10^6	450	2	0.05	360	280	25	2.0×10^{-5}	1.08	4.23
7	1.0×10^6	500	2	0.05	360	280	25	2.0×10^{-5}	1.02	0.97
8	1.0×10^6	1000	2	0.05	360	280	25	2.0×10^{-5}	1.02	1.1
9	1.0×10^6	2000	2	0.05	640	280	25	5.0×10^{-6}	1.02	1.4
10	1.0×10^6	5000	2	0.05	800	280	25	2.5×10^{-6}	1.02	2.6
11	3.0×10^6	0	2	0.05	360	280	25	5.0×10^{-4}	9.23	334.2
12	3.0×10^6	200	2	0.05	360	280	25	1.0×10^{-4}	9.23	335.7
13	3.0×10^6	400	2	0.05	360	280	25	5.0×10^{-5}	9.74	355.0
14	3.0×10^6	500	2	0.05	360	280	25	2.0×10^{-5}	10.0	362.5
15	3.0×10^6	600	2	0.05	360	280	25	2.0×10^{-5}	6.64	126.0
16	3.0×10^6	700	2	0.05	360	280	25	2.0×10^{-5}	5.97	100.5
17	3.0×10^6	800	2	0.05	360	280	25	2.0×10^{-5}	1.02	1.2
18	3.0×10^6	1000	2	0.05	360	280	25	2.0×10^{-5}	1.02	1.2
19	3.0×10^6	2000	2	0.05	640	280	25	1.0×10^{-5}	1.02	1.4
20	3.0×10^6	5000	2	0.05	800	280	25	4.0×10^{-6}	1.02	2.5
21	1.0×10^7	0	2	0.05	360	280	25	2.0×10^{-4}	12.3	613.0
22	1.0×10^7	200	2	0.05	360	280	25	2.0×10^{-4}	12.3	623.5
23	1.0×10^7	400	2	0.05	360	280	25	1.0×10^{-4}	11.9	655.0
24	1.0×10^7	600	2	0.05	360	280	25	5.0×10^{-5}	12.2	670.0
25	1.0×10^7	1000	2	0.05	480	400	39	2.0×10^{-5}	13.7	715.0
26	1.0×10^7	1150	2	0.05	480	400	39	2.0×10^{-5}	13.8	736.0
27	1.0×10^7	1300	2	0.05	480	400	39	2.0×10^{-5}	8.60	225.0
28	1.0×10^7	1400	2	0.05	480	400	39	2.0×10^{-5}	8.20	201.0
29	1.0×10^7	1500	2	0.05	480	400	39	2.0×10^{-5}	1.02	1.7
30	1.0×10^7	2000	2	0.05	640	400	39	1.0×10^{-5}	1.02	1.9
31	1.0×10^7	5000	2	0.05	800	400	39	5.0×10^{-6}	1.02	2.8
32	3.0×10^7	0	2	0.05	480	400	39	2.0×10^{-4}	15.9	1211
33	3.0×10^7	200	2	0.05	480	400	39	2.0×10^{-4}	15.9	1210
34	3.0×10^7	400	2	0.05	480	400	39	1.0×10^{-4}	15.9	1215
35	3.0×10^7	600	2	0.05	480	400	39	1.0×10^{-4}	16.4	1230
36	3.0×10^7	1000	2	0.05	480	400	39	5.0×10^{-5}	17.4	1254
37	3.0×10^7	1500	2	0.05	640	400	39	5.0×10^{-5}	18.7	1317
38	3.0×10^7	2000	2	0.05	640	400	39	2.5×10^{-5}	20.2	1389
39	3.0×10^7	2500	2	0.05	640	400	39	1.0×10^{-5}	11.7	397.0
40	3.0×10^7	2750	2	0.05	640	400	39	1.0×10^{-5}	10.0	330.0
41	3.0×10^7	3000	2	0.05	640	400	39	1.0×10^{-5}	1.02	2.3
42	3.0×10^7	5000	2	0.05	800	400	39	1.0×10^{-5}	1.02	2.9

Table 2. Cases at $\Gamma = 2$ and $h = 0.05$.

horizontal cross section for smooth cases, the Nusselt number can also be written as the volume- and time-averaged heat flux, i.e. $Nu = \sqrt{Ra\,Pr}\,\langle w\theta\rangle_{t,v} + 1$. Then we obtain $\bar{P}_{buo} = (Nu-1)/\sqrt{Ra\,Pr}$. Hence the total production $\bar{P}$ in the buoyancy-dominant regime can be estimated by $\bar{P} \sim Nu/\sqrt{Ra\,Pr}$ as $\bar{P} \sim \bar{P}_{buo}$. Second, using the divergence theorem, $\bar{P}_{shear}$ can be rewritten as $\bar{P}_{shear} = \frac{1}{2}\langle\partial_z|\boldsymbol{u}|^2\rangle_{t,top}/\sqrt{Ra/Pr} - \frac{1}{2}\langle\partial_z|\boldsymbol{u}|^2\rangle_{t,bot}/\sqrt{Ra/Pr}$,

No.	Ra	Re_w	Γ	h	N_x	N_z	N_h	δt	Nu	Re_z
1	1.0×10^6	0	2	0.1	360	320	66	1.0×10^{-3}	7.48	162.7
2	1.0×10^6	200	2	0.1	360	320	66	1.0×10^{-4}	7.20	172.0
3	1.0×10^6	300	2	0.1	360	320	66	5.0×10^{-5}	7.43	174.5
4	1.0×10^6	350	2	0.1	360	320	66	2.0×10^{-5}	4.90	62.0
5	1.0×10^6	400	2	0.1	360	320	66	2.0×10^{-5}	3.00	32.0
6	1.0×10^6	450	2	0.1	360	320	66	2.0×10^{-5}	1.07	3.2
7	1.0×10^6	1000	2	0.1	360	320	66	1.0×10^{-5}	1.06	1.9
8	1.0×10^6	2000	2	0.1	640	320	66	5.0×10^{-6}	1.06	2.9
9	1.0×10^6	5000	2	0.1	800	320	66	2.5×10^{-6}	1.07	5.2
10	2.2×10^6	0	2	0.1	360	320	66	5.0×10^{-4}	8.49	245.7
11	2.2×10^6	200	2	0.1	360	320	66	1.0×10^{-4}	8.76	254.6
12	2.2×10^6	400	2	0.1	360	320	66	5.0×10^{-5}	9.03	277.0
13	2.2×10^6	500	2	0.1	360	320	66	2.0×10^{-5}	9.45	283.0
14	2.2×10^6	600	2	0.1	360	320	66	2.0×10^{-5}	5.30	71.0
15	2.2×10^6	700	2	0.1	360	320	66	2.0×10^{-5}	1.06	1.3
16	2.2×10^6	1000	2	0.1	360	320	66	1.0×10^{-5}	1.06	1.8
17	2.2×10^6	2000	2	0.1	640	320	66	1.0×10^{-5}	1.06	2.9
18	2.2×10^6	5000	2	0.1	800	320	66	2.5×10^{-6}	1.06	5.2
19	4.6×10^6	0	2	0.1	360	320	66	5.0×10^{-4}	9.59	361.2
20	4.6×10^6	200	2	0.1	360	320	66	1.0×10^{-4}	10.3	367.7
21	4.6×10^6	400	2	0.1	360	320	66	5.0×10^{-5}	10.8	394.0
22	4.6×10^6	600	2	0.1	360	320	66	5.0×10^{-5}	11.5	424.9
23	4.6×10^6	800	2	0.1	480	432	74	2.0×10^{-5}	11.6	458.2
24	4.6×10^6	900	2	0.1	480	432	74	2.0×10^{-5}	6.70	119.0
25	4.6×10^6	1000	2	0.1	480	432	74	2.0×10^{-5}	1.06	1.6
26	4.6×10^6	2000	2	0.1	640	432	74	1.0×10^{-5}	1.06	2.8
27	4.6×10^6	5000	2	0.1	800	432	74	4.0×10^{-6}	1.06	5.2
28	1.0×10^7	0	2	0.1	480	320	66	2.0×10^{-4}	11.8	553.0
29	1.0×10^7	200	2	0.1	480	320	66	1.0×10^{-4}	12.1	556.8
30	1.0×10^7	400	2	0.1	480	320	66	1.0×10^{-4}	12.2	594.0
31	1.0×10^7	600	2	0.1	480	320	66	5.0×10^{-5}	12.7	625.5
32	1.0×10^7	1000	2	0.1	480	320	66	2.0×10^{-5}	14.3	671.2
33	1.0×10^7	1300	2	0.1	640	432	74	2.0×10^{-5}	14.9	719.0
34	1.0×10^7	1500	2	0.1	640	432	74	2.0×10^{-5}	6.86	140.0
35	1.0×10^7	1700	2	0.1	640	432	74	2.0×10^{-5}	1.06	2.6
36	1.0×10^7	2000	2	0.1	640	432	74	1.0×10^{-5}	1.06	2.5
37	1.0×10^7	5000	2	0.1	800	432	74	5.0×10^{-6}	1.06	5.3
38	2.2×10^7	0	2	0.1	480	432	74	2.0×10^{-4}	14.4	917.0
39	2.2×10^7	200	2	0.1	480	432	74	2.0×10^{-4}	15.3	859.1
40	2.2×10^7	400	2	0.1	480	432	74	1.0×10^{-4}	15.5	900.5
41	2.2×10^7	600	2	0.1	480	432	74	1.0×10^{-4}	15.8	950.3
42	2.2×10^7	1000	2	0.1	480	432	74	5.0×10^{-5}	17.4	1010
43	2.2×10^7	1500	2	0.1	800	512	100	2.0×10^{-5}	19.5	1088
44	2.2×10^7	2000	2	0.1	800	512	100	2.0×10^{-5}	22.4	1209
45	2.2×10^7	2390	2	0.1	1024	640	137	2.0×10^{-5}	9.00	237.0
46	2.2×10^7	2700	2	0.1	1024	640	137	1.0×10^{-5}	1.06	5.0
47	2.2×10^7	5000	2	0.1	1024	640	137	1.0×10^{-5}	1.06	5.8
48	4.6×10^7	0	2	0.1	480	432	74	2.0×10^{-4}	19.6	1399
49	4.6×10^7	200	2	0.1	480	432	74	2.0×10^{-4}	19.8	1422
50	4.6×10^7	400	2	0.1	480	432	74	1.0×10^{-5}	20.3	1410

Table 3. For caption see next page.

No.	Ra	Re_w	Γ	h	N_x	N_z	N_h	δt	Nu	Re_z
51	4.6×10^7	600	2	0.1	480	432	74	1.0×10^{-5}	21.1	1447
52	4.6×10^7	1000	2	0.1	480	432	74	5.0×10^{-5}	22.1	1490
53	4.6×10^7	1500	2	0.1	800	512	100	2.0×10^{-5}	24.0	1588
54	4.6×10^7	2000	2	0.1	800	512	100	2.0×10^{-5}	26.4	1705
55	4.6×10^7	3000	2	0.1	1024	640	137	1.0×10^{-5}	33.1	1984
56	4.6×10^7	3765	2	0.1	1024	800	186	1.0×10^{-5}	13.0	400.0
57	4.6×10^7	4000	2	0.1	1024	800	186	1.0×10^{-5}	1.06	6.3
58	4.6×10^7	5000	2	0.1	1024	800	186	1.0×10^{-5}	1.06	7.6
59	1.0×10^8	0	2	0.1	640	512	100	1.0×10^{-4}	28.1	2284
60	1.0×10^8	200	2	0.1	640	512	100	1.0×10^{-4}	28.5	2296
61	1.0×10^8	400	2	0.1	640	512	100	1.0×10^{-4}	28.5	2315
62	1.0×10^8	600	2	0.1	640	512	100	1.0×10^{-4}	28.8	2340
63	1.0×10^8	1000	2	0.1	640	512	100	8.0×10^{-5}	30.7	2415
64	1.0×10^8	1500	2	0.1	800	512	100	5.0×10^{-5}	33.3	2567
65	1.0×10^8	2000	2	0.1	800	512	100	2.0×10^{-5}	35.2	2712
66	1.0×10^8	3000	2	0.1	1024	640	137	1.0×10^{-5}	40.3	2983
67	1.0×10^8	4000	2	0.1	1024	800	186	1.0×10^{-5}	45.4	3267
68	1.0×10^8	5000	2	0.1	640	800	186	1.0×10^{-5}	50.1	3580
69	1.0×10^8	5000	2	0.1	800	800	186	1.0×10^{-5}	49.9	3575
70	1.0×10^8	5000	2	0.1	1024	800	186	1.0×10^{-5}	49.5	3565
71	1.0×10^8	5000	2	0.1	1280	800	186	1.0×10^{-5}	49.5	3562
72	1.0×10^8	5000	2	0.1	1024	512	100	1.0×10^{-5}	51.1	3617
73	1.0×10^8	5000	2	0.1	1024	640	137	1.0×10^{-5}	50.4	3592
74	1.0×10^8	5000	2	0.1	1024	960	223	1.0×10^{-5}	49.5	3560

Table 3. Cases at $\Gamma = 2$ and $h = 0.1$.

where $\langle\cdot\rangle_{top}$ (or $\langle\cdot\rangle_{bot}$) represents the average over the top plate (or the bottom plate). As $\partial_z|\boldsymbol{u}|^2 = 2u\partial_z u + 2w\partial_z w$, $u = u_w$ on the top plate, $u = -u_w$ on the bottom plate, and $w = 0$ on both plates, we obtain $\bar{P}_{shear} = 2u_w\partial_z U/\sqrt{Ra/Pr}$, where $\partial_z U = \langle\partial_z u\rangle_{t,bot}$ (or $\langle\partial_z u\rangle_{t,top}$) means the partial derivative of horizontal (x-) velocity in the vertical (z-) direction on the plates. Assuming $\partial_z U \sim (u_w - (-u_w))/1$ from the dimensional analysis, namely $\partial_z U \sim 2u_w$, the total production in the shear-dominant regime is approximated by $\bar{P} \sim 4u_w^2/\sqrt{Ra/Pr} \sim Re_w^2(Ra/Pr)^{-3/2}$ as $\bar{P} \sim \bar{P}_{shear}$. Finally, the change of $\bar{P}$ with respect to Re_w is continuous. To determine the transitional scaling, we connect the total production $\bar{P} \sim Nu/\sqrt{Ra\,Pr}$ in the buoyancy-dominant regime and $\bar{P} \sim Re_w^2(Ra/Pr)^{-3/2}$ in the shear-dominant regime, yielding the relation of the critical shear Reynolds number $Re_{w,cr}$ in the transitional regime, i.e. $Re_{w,cr} \sim Nu^{1/2}Ra^{1/2}Pr^{-1}$. Together with $Nu \sim Ra^{2/7}$ for two-dimensional thermal convection with periodic boundary conditions (Ahlers *et al.* 2009), we obtain the transitional scaling

$$Re_{w,cr} \sim Ra^{9/14}. \tag{3.2}$$

From all our numerical results shown in figures 6, 12 and 14, it is seen that our predicted scaling $Re_{w,cr} \sim Ra^{9/14}$ is able to characterize the transitional behaviour in two-dimensional sheared thermal convection.

No.	Ra	Re_w	Γ	h	N_x	N_z	N_h	δt	Nu	Re_z
1	1.0×10^6	0	2	0.2	360	360	83	1.0×10^{-3}	7.28	129.1
2	1.0×10^6	200	2	0.2	360	360	83	1.0×10^{-4}	7.32	137.4
3	1.0×10^6	300	2	0.2	360	360	83	5.0×10^{-5}	7.30	143.2
4	1.0×10^6	350	2	0.2	360	360	83	2.5×10^{-5}	4.57	48.6
5	1.0×10^6	400	2	0.2	360	360	83	2.5×10^{-5}	2.29	19.6
6	1.0×10^6	450	2	0.2	360	360	83	2.0×10^{-5}	1.17	1.19
7	1.0×10^6	500	2	0.2	360	360	83	2.0×10^{-5}	1.17	1.28
8	1.0×10^6	1000	2	0.2	360	360	83	2.0×10^{-5}	1.17	2.4
9	1.0×10^6	2000	2	0.2	640	360	83	5.0×10^{-6}	1.17	5.6
10	1.0×10^6	5000	2	0.2	800	360	83	2.5×10^{-6}	1.17	23.6
11	3.0×10^6	0	2	0.2	360	360	83	5.0×10^{-4}	9.08	229.0
12	3.0×10^6	200	2	0.2	360	360	83	1.0×10^{-4}	9.68	237.0
13	3.0×10^6	400	2	0.2	360	360	83	5.0×10^{-5}	10.7	255.2
14	3.0×10^6	500	2	0.2	360	360	83	2.0×10^{-5}	11.1	267.0
15	3.0×10^6	600	2	0.2	360	360	83	2.0×10^{-5}	11.2	284.1
16	3.0×10^6	700	2	0.2	360	360	83	2.0×10^{-5}	5.00	66.00
17	3.0×10^6	800	2	0.2	360	360	83	2.0×10^{-5}	1.18	2.1
18	3.0×10^6	1000	2	0.2	360	360	83	2.0×10^{-5}	1.18	2.4
19	3.0×10^6	2000	2	0.2	640	360	83	1.0×10^{-5}	1.18	5.6
20	3.0×10^6	5000	2	0.2	800	360	83	4.0×10^{-6}	1.18	23.2
21	1.0×10^7	0	2	0.2	480	576	145	2.0×10^{-4}	12.0	443.5
22	1.0×10^7	200	2	0.2	480	576	145	1.0×10^{-4}	13.2	448.5
23	1.0×10^7	400	2	0.2	480	576	145	1.0×10^{-4}	13.8	467.7
24	1.0×10^7	600	2	0.2	480	576	145	5.0×10^{-5}	13.6	515.8
25	1.0×10^7	1000	2	0.2	480	576	145	2.0×10^{-5}	15.2	567.0
26	1.0×10^7	1500	2	0.2	480	576	145	2.0×10^{-5}	17.0	655.0
27	1.0×10^7	1750	2	0.2	480	576	145	2.0×10^{-5}	1.18	5.5
28	1.0×10^7	2000	2	0.2	640	576	145	1.0×10^{-5}	1.18	5.6
29	1.0×10^7	5000	2	0.2	800	576	145	5.0×10^{-6}	1.18	23.1
30	3.0×10^7	0	2	0.2	480	576	145	2.0×10^{-4}	17.8	898.0
31	3.0×10^7	200	2	0.2	480	576	145	2.0×10^{-4}	18.2	897.0
32	3.0×10^7	400	2	0.2	480	576	145	1.0×10^{-4}	19.1	900.4
33	3.0×10^7	600	2	0.2	480	576	145	1.0×10^{-4}	19.6	926.8
34	3.0×10^7	1000	2	0.2	480	576	145	5.0×10^{-5}	20.8	978.5
35	3.0×10^7	1500	2	0.2	480	576	145	2.5×10^{-5}	23.0	1055
36	3.0×10^7	2000	2	0.2	480	576	145	2.5×10^{-5}	26.2	1162
37	3.0×10^7	2500	2	0.2	800	576	145	1.0×10^{-5}	30.9	1314
38	3.0×10^7	2750	2	0.2	800	576	145	1.0×10^{-5}	33.3	1396
39	3.0×10^7	3000	2	0.2	1024	576	145	1.0×10^{-5}	1.18	11.5
40	3.0×10^7	5000	2	0.2	1024	576	145	1.0×10^{-5}	1.18	23.2

Table 4. Cases at $\Gamma = 2$ and $h = 0.2$.

4. Conclusion

In summary, we have carried out a series of DNS of wall-sheared RB convection over rough plates over $1.0 \times 10^6 \leq Ra \leq 1.0 \times 10^8$, $0 \leq Re_w \leq 5000$, $2 \leq \Gamma \leq 4\pi$ and $0 \leq h \leq 0.2$. With the critical shear Reynolds number $Re_{w,cr}$, three flow states can be categorized: the buoyancy-dominant, transitional and shear-dominant regimes. In the buoyancy-dominant regime, flow structures resemble large-scale stretched convective rolls as those in standard RB convection, and the number of LSRs decreases with increasing

No.	Ra	Re_w	Γ	h	N_x	N_z	N_h	δt	Nu	Re_z
1	1.0×10^6	0	2π	0.1	1008	336	57	5.0×10^{-4}	6.89	191.7
2	1.0×10^6	200	2π	0.1	1008	336	57	8.0×10^{-5}	7.18	166.4
3	1.0×10^6	400	2π	0.1	1008	336	57	5.0×10^{-5}	6.16	91.7
4	1.0×10^6	450	2π	0.1	1008	336	57	5.0×10^{-5}	6.31	95.1
5	1.0×10^6	475	2π	0.1	1008	336	57	2.5×10^{-5}	6.35	97.3
6	1.0×10^6	500	2π	0.1	1008	336	57	2.5×10^{-5}	1.70	12.5
7	1.0×10^6	500	2π	0.1	1536	432	74	2.5×10^{-5}	1.80	13.4
8	1.0×10^6	525	2π	0.1	1008	336	57	2.5×10^{-5}	1.24	5.8
9	1.0×10^6	550	2π	0.1	1008	336	57	2.5×10^{-5}	1.17	4.0
10	1.0×10^6	550	2π	0.1	1008	336	57	2.5×10^{-5}	1.17	4.0
11	1.0×10^6	575	2π	0.1	1008	336	57	2.5×10^{-5}	1.06	1.19
12	1.0×10^6	600	2π	0.1	1008	336	57	2.5×10^{-5}	1.06	1.2
13	1.0×10^6	1000	2π	0.1	1008	336	57	2.5×10^{-5}	1.06	1.8
14	1.0×10^6	2000	2π	0.1	1008	336	57	1.0×10^{-5}	1.06	2.8
15	1.0×10^6	5000	2π	0.1	1536	336	57	4.0×10^{-6}	1.06	5.2
16	3.0×10^6	0	2π	0.1	1008	336	57	5.0×10^{-4}	8.82	279.6
17	3.0×10^6	200	2π	0.1	1008	336	57	1.0×10^{-4}	9.43	284.9
18	3.0×10^6	500	2π	0.1	1008	336	57	5.0×10^{-5}	9.40	237.9
19	3.0×10^6	1000	2π	0.1	1008	336	57	2.5×10^{-5}	8.50	167.0
20	3.0×10^6	1050	2π	0.1	1008	336	57	2.5×10^{-5}	9.43	183.4
21	3.0×10^6	1100	2π	0.1	1008	336	57	2.5×10^{-5}	1.06	1.9
22	3.0×10^6	1250	2π	0.1	1008	336	57	2.5×10^{-5}	1.06	2.1
23	3.0×10^6	2000	2π	0.1	1008	336	57	1.0×10^{-5}	1.06	2.8
24	3.0×10^6	5000	2π	0.1	1536	336	57	5.0×10^{-6}	1.06	5.2
25	1.0×10^7	0	2π	0.1	1536	432	74	2.0×10^{-4}	11.9	522.5
26	1.0×10^7	200	2π	0.1	1536	432	74	1.0×10^{-4}	12.0	537.1
27	1.0×10^7	400	2π	0.1	1536	432	74	1.0×10^{-4}	13.5	539.5
28	1.0×10^7	1000	2π	0.1	1536	432	74	5.0×10^{-5}	14.1	650.0
29	1.0×10^7	1500	2π	0.1	1536	432	74	5.0×10^{-5}	15.9	736.4
30	1.0×10^7	2000	2π	0.1	1536	432	74	2.5×10^{-5}	15.4	587.0
31	1.0×10^7	2150	2π	0.1	1536	432	74	2.5×10^{-5}	15.5	590.0
32	1.0×10^7	2225	2π	0.1	1536	432	74	2.5×10^{-5}	15.6	596.0
33	1.0×10^7	2300	2π	0.1	1536	432	74	2.5×10^{-5}	1.06	3.8
34	1.0×10^7	2500	2π	0.1	1536	432	74	1.0×10^{-5}	1.06	4.0
35	1.0×10^7	5000	2π	0.1	2016	432	74	8.0×10^{-6}	1.06	5.5
36	3.0×10^7	0	2π	0.1	1536	432	74	2.0×10^{-4}	16.5	1040
37	3.0×10^7	200	2π	0.1	1536	432	74	1.0×10^{-4}	17.4	1284
38	3.0×10^7	400	2π	0.1	1536	432	74	1.0×10^{-4}	18.2	1296
39	3.0×10^7	1000	2π	0.1	1536	432	74	1.0×10^{-4}	18.8	1125
40	3.0×10^7	2000	2π	0.1	1536	432	74	5.0×10^{-5}	23.7	1330
41	3.0×10^7	3000	2π	0.1	2016	576	110	2.5×10^{-5}	28.7	1540
42	3.0×10^7	4000	2π	0.1	2016	576	110	1.0×10^{-5}	31.3	1660
43	3.0×10^7	4500	2π	0.1	2016	576	110	1.0×10^{-5}	32.2	1720
44	3.0×10^7	4500	2π	0.1	2496	784	166	1.0×10^{-5}	32.3	1743
45	3.0×10^7	4750	2π	0.1	2016	576	110	1.0×10^{-5}	32.1	1698
46	3.0×10^7	5000	2π	0.1	2016	576	110	1.0×10^{-5}	1.06	6.4

Table 5. Cases at $\Gamma = 2\pi$ and $h = 0.1$.

No.	Ra	Re_w	Γ	h	N_x	N_z	N_h	δt	Nu	Re_z
1	1.0×10^6	0	4π	0.1	2016	336	57	5.0×10^{-4}	7.54	156.6
2	1.0×10^6	200	4π	0.1	2016	336	57	8.0×10^{-5}	7.38	144.5
3	1.0×10^6	475	4π	0.1	2016	336	57	5.0×10^{-5}	5.62	60.3
4	1.0×10^6	500	4π	0.1	2016	336	57	5.0×10^{-5}	5.64	62.7
5	1.0×10^6	600	4π	0.1	2016	336	57	2.5×10^{-5}	5.57	69.3
6	1.0×10^6	650	4π	0.1	2016	336	57	2.5×10^{-5}	1.19	3.5
7	1.0×10^6	675	4π	0.1	2016	336	57	2.5×10^{-5}	1.19	3.7
8	1.0×10^6	700	4π	0.1	2016	336	57	2.5×10^{-5}	1.06	1.4
9	1.0×10^6	1000	4π	0.1	2016	336	57	2.5×10^{-5}	1.06	1.8
10	1.0×10^6	2000	4π	0.1	2016	336	57	1.0×10^{-5}	1.06	2.8
11	1.0×10^6	5000	4π	0.1	3024	336	57	4.0×10^{-6}	1.06	5.2
12	3.0×10^6	0	4π	0.1	2016	336	57	5.0×10^{-4}	9.03	333.2
13	3.0×10^6	200	4π	0.1	2016	336	57	1.0×10^{-4}	9.28	247.7
14	3.0×10^6	400	4π	0.1	2016	336	57	5.0×10^{-5}	9.88	264.3
15	3.0×10^6	1000	4π	0.1	2016	336	57	2.5×10^{-5}	8.70	170.3
16	3.0×10^6	1050	4π	0.1	2016	336	57	2.5×10^{-5}	1.06	2.2
17	3.0×10^6	1100	4π	0.1	2016	336	57	2.5×10^{-5}	1.06	1.8
18	3.0×10^6	1150	4π	0.1	2016	336	57	2.5×10^{-5}	1.06	1.8
19	3.0×10^6	2000	4π	0.1	2016	336	57	1.0×10^{-5}	1.06	2.8
20	3.0×10^6	5000	4π	0.1	3024	336	57	5.0×10^{-6}	1.06	5.2
21	1.0×10^7	0	4π	0.1	3024	432	74	2.0×10^{-4}	12.5	646.2
22	1.0×10^7	200	4π	0.1	3024	432	74	1.0×10^{-4}	12.3	527.0
23	1.0×10^7	400	4π	0.1	3024	432	74	1.0×10^{-4}	13.0	627.0
24	1.0×10^7	600	4π	0.1	3024	432	74	1.0×10^{-4}	14.2	567.7
25	1.0×10^7	1000	4π	0.1	3024	432	74	5.0×10^{-5}	13.6	548.5
26	1.0×10^7	1500	4π	0.1	3024	432	74	5.0×10^{-5}	14.9	609.5
27	1.0×10^7	2000	4π	0.1	3024	432	74	2.5×10^{-5}	15.3	589.3
28	1.0×10^7	2300	4π	0.1	3024	432	74	2.5×10^{-5}	15.1	563.0
29	1.0×10^7	2350	4π	0.1	3024	432	74	2.5×10^{-5}	15.2	568.2
30	1.0×10^7	2400	4π	0.1	3024	432	74	2.5×10^{-5}	1.06	3.1
31	1.0×10^7	2500	4π	0.1	3024	432	74	1.0×10^{-5}	1.06	3.2
32	1.0×10^7	5000	4π	0.1	4032	432	74	8.0×10^{-6}	1.06	5.4
33	3.0×10^7	0	4π	0.1	3024	432	74	2.0×10^{-4}	17.5	1230
34	3.0×10^7	200	4π	0.1	3024	432	74	1.0×10^{-4}	17.0	997.4
35	3.0×10^7	400	4π	0.1	3024	432	74	1.0×10^{-4}	17.1	1013
36	3.0×10^7	1000	4π	0.1	3024	432	74	1.0×10^{-4}	18.7	1115
37	3.0×10^7	3000	4π	0.1	4032	576	110	2.5×10^{-5}	28.1	1509
38	3.0×10^7	5000	4π	0.1	4032	576	110	1.0×10^{-5}	32.7	1745
39	3.0×10^7	5250	4π	0.1	4032	576	110	1.0×10^{-5}	1.06	6.5
40	3.0×10^7	5500	4π	0.1	4032	576	110	1.0×10^{-5}	1.06	6.5

Table 6. Cases at $\Gamma = 4\pi$ and $h = 0.1$.

Re_w for large Γ. When Re_w is around the critical value, a sharp transition takes place abruptly and the corresponding Nu decrease dramatically. In the shear-dominant regime, the flow is laminar Couette flow for the velocity field and pure conduction for temperature.

Making use of the kinetic energy transport equation, the critical shear Reynolds number $Re_{w,cr}$ can be estimated by the crossover between the total production in the buoyancy-dominant and shear-dominant regimes, i.e. $Re_{w,cr} \sim Ra^{9/14}$, which can well characterize the observed transition behaviour. It is found that both the aspect ratio and

roughness height have only a slight influence on the transitional scaling. The region of the transitional regime shrinks with a larger roughness height h.

In the buoyancy-dominant regime, the physical reason for the heat-transport enhancement is that the moving rough plates serve as conveyor belts and increase the chances of interactions between the LSC and secondary flows within each cavity between rough elements. This efficiently pumps the trapped hot (cold) fluids out of the cavities, thins thermal BLs, strengthens the LSC, and consequently enhances the global heat-transfer efficiency of the system.

Supplementary movies. Supplementary movies are available at https://doi.org/10.1017/jfm.2021.1111.

Funding. This work was supported by the Natural Science Foundation of China under grant nos 11988102, 11825204, 92052201, 12032016, 11732010, 12102246 and 91852202, the Program of Shanghai Academic Research Leader under grant no. 19XD1421400, the Science and Technology Innovation Plan of Shanghai Science and Technology Commission (STCSM) under project nos. 19JC1412802, the Shanghai Pujiang Program under grant no. 21PJ1404400, and the China Postdoctoral Science Foundation under grant no. 2020M681259.

Declaration of interests. The authors report no conflict of interest.

Author ORCIDs.
Quan Zhou https://orcid.org/0000-0002-0411-7228.

Appendix A. Numerical details

Here, we provide values of the control parameters and the numerical results of the simulations in our research, which are divided into six tables 1, 2, 3, 4, 5, 6 by the aspect ratio Γ and dimensionless roughness height h. N_x and N_z are respectively the grid resolution in the horizontal and vertical directions. δt is the dimensionless time step of each case. The Prandtl number Pr and dimensionless roughness wavelength λ are respectively fixed to 1 and 0.2 in all simulations.

References

Abtahi, A. & Floryan, J.M. 2017 Natural convection and thermal drift. *J. Fluid Mech.* **826**, 553–582.

Ahlers, G., Grossmann, S. & Lohse, D. 2009 Heat transfer and large scale dynamics in turbulent Rayleigh–Bénard convection. *Rev. Mod. Phys.* **81** (2), 503–537.

Blass, A., Tabak, P., Verzicco, R., Stevens, R.J.A.M. & Lohse, D. 2021 The effect of Prandtl number on turbulent sheared thermal convection. *J. Fluid Mech.* **910**, A37.

Blass, A., Zhu, X.J., Verzicco, R., Lohse, D. & Stevens, R.J.A.M. 2020 Flow organization and heat transfer in turbulent wall sheared thermal convection. *J. Fluid Mech.* **897**, A22.

Bluestein, H.B. 2013 *Severe Convective Storms and Tornadoes*, vol. 10, pp. 95–104. Springer.

Chillà, F. & Schumacher, J. 2012 New perspectives in turbulent Rayleigh–Bénard convection. *Eur. Phys. J.* E **35** (7), 58.

Domaradzki, J.A. & Metcalfe, R.W. 1988 Direct numerical simulations of the effects of shear on turbulent Rayleigh–Bénard convection. *J. Fluid Mech.* **193**, 499–531.

Dong, D.L., Wang, B.F., Dong, Y.H., Huang, Y.X., Jiang, N., Liu, Y.L., Lu, Z.M., Qiu, X., Tang, Z.Q. & Zhou, Q. 2020 Influence of spatial arrangements of roughness elements on turbulent Rayleigh–Bénard convection. *Phys. Fluids* **32** (4), 045114.

Du, Y.B. & Tong, P. 1998 Enhanced heat transport in turbulent convection over a rough surface. *Phys. Rev. Lett.* **81** (5), 987–990.

Du, Y.B. & Tong, P. 2000 Turbulent thermal convection in a cell with ordered rough boundaries. *J. Fluid Mech.* **407**, 57–84.

Fadlun, E.A., Verzicco, R., Orlandi, P. & Mohd-Yusof, J. 2000 Combined immersed-boundary finite-difference methods for three-dimensional complex flow simulations. *J. Comput. Phys.* **161** (1), 35–60.

GROSSMANN, S. & LOHSE, D. 2000 Scaling in thermal convection: a unifying theory. *J. Fluid Mech.* **407**, 27–56.

HOSSAIN, M.Z. & FLORYAN, J.M. 2020 On the role of surface grooves in the reduction of pressure losses in heated channels. *Phys. Fluids* **32** (8), 083610.

HUANG, S.-D., KACZOROWSKI, M., NI, R. & XIA, K.-Q. 2013 Confinement-induced heat transport enhancement in turbulent thermal convection. *Phys. Rev. Lett.* **111**, 104501.

JIANG, H.C., ZHU, X.J., MATHAI, V., VERZICCO, R., LOHSE, D. & SUN, C. 2018 Controlling heat transport and flow structures in thermal turbulence using ratchet surfaces. *Phys. Rev. Lett.* **120** (4), 044501.

LANGHAM, J., EAVES, T.S. & KERSWELL, R.R. 2020 Stably stratified exact coherent structures in shear flow: the effect of Prandtl number. *J. Fluid Mech.* **882**, A10.

LOHSE, D. & XIA, K.Q. 2010 Small-scale properties of turbulent Rayleigh–Bénard convection. *Annu. Rev. Fluid Mech.* **42** (1), 335–364.

MACDONALD, M., HUTCHINS, N., LOHSE, D. & CHUNG, D. 2019 Heat transfer in rough-wall turbulent thermal convection in the ultimate regime. *Phys. Rev. Fluids* **4** (7), 071501.

PIROZZOLI, S., BERNARDINI, M., VERZICCO, R. & ORLANDI, P. 2017 Mixed convection in turbulent channels with unstable stratification. *J. Fluid Mech.* **821**, 482–516.

VAN DER POEL, E.P., VERZICCO, R., GROSSMANN, S. & LOHSE, D. 2015 Plume emission statistics in turbulent Rayleigh–Bénard convection. *J. Fluid Mech.* **772**, 5–15.

ROCHE, P.E., CASTAING, B., CHABAUD, B. & HÉBRAL, B. 2001 Observation of the 1/2 power law in Rayleigh–Bénard convection. *Phys. Rev.* E **63** (4), 045303.

RUSAOUËN, E., LIOT, O., CASTAING, B., SALORT, J. & CHILLÀ, F. 2018 Thermal transfer in Rayleigh–Bénard cell with smooth or rough boundaries. *J. Fluid Mech.* **837**, 443–460.

SCAGLIARINI, A., EINARSSON, H., GYLFASON, Á. & TOSCHI, F. 2015 Law of the wall in an unstably stratified turbulent channel flow. *J. Fluid Mech.* **781**, R5.

SCAGLIARINI, A., GYLFASON, Á. & TOSCHI, F. 2014 Heat-flux scaling in turbulent Rayleigh–Bénard convection with an imposed longitudinal wind. *Phys. Rev.* E **89** (4), 043012.

SHEN, Y., TONG, P. & XIA, K.Q. 1996 Turbulent convection over rough surfaces. *Phys. Rev. Lett.* **76** (6), 908–911.

SHISHKINA, O. & WAGNER, C. 2011 Modelling the influence of wall roughness on heat transfer in thermal convection. *J. Fluid Mech.* **686**, 568–582.

SOLOMON, T.H. & GOLLUB, J.P. 1990 Sheared boundary layers in turbulent Rayleigh–Bénard convection. *Phys. Rev. Lett.* **64** (20), 2382–2385.

TISSERAND, J.C., CREYSSELS, M., GASTEUIL, Y., PABIOU, H., GIBERT, M., CASTAING, B. & CHILLÀ, F. 2011 Comparison between rough and smooth plates within the same Rayleigh–Bénard cell. *Phys. Fluids* **23** (1), 015105.

TUMMERS, M.J. & STEUNEBRINK, M. 2019 Effect of surface roughness on heat transfer in Rayleigh–Bénard convection. *Intl J. Heat Mass Transfer* **139**, 1056–1064.

VISHNU, R. & SAMEEN, A. 2020 Heat transfer scaling in natural convection with shear due to rotation. *Phys. Rev. Fluids* **5** (11), 113504.

WAGNER, S. & SHISHKINA, O. 2015 Heat flux enhancement by regular surface roughness in turbulent thermal convection. *J. Fluid Mech.* **763**, 109–135.

WANG, B.F., ZHOU, Q. & SUN, C. 2020 Vibration-induced boundary-layer destabilization achieves massive heat-transport enhancement. *Sci. Adv.* **6** (21), eaaz8239.

WEI, P., CHAN, T.S., NI, R., ZHAO, X.Z. & XIA, K.Q. 2014 Heat transport properties of plates with smooth and rough surfaces in turbulent thermal convection. *J. Fluid Mech.* **740**, 28–46.

XIE, Y.C. & XIA, K.Q. 2017 Turbulent thermal convection over rough plates with varying roughness geometries. *J. Fluid Mech.* **825**, 573–599.

YANG, J.L., ZHANG, Y.Z., JIN, T.C., DONG, Y.H., WANG, B.F. & ZHOU, Q. 2021 The *Pr*-dependence of the critical roughness height in two-dimensional turbulent Rayleigh–Bénard convection. *J. Fluid Mech.* **911**, A52.

ZHANG, Y.Z., SUN, C., BAO, Y. & ZHOU, Q. 2018 How surface roughness reduces heat transport for small roughness heights in turbulent Rayleigh–Bénard convection. *J. Fluid Mech.* **836**, R2.

ZHANG, Y.Z., XIA, S.N., DONG, Y.H., WANG, B.F. & ZHOU, Q. 2019 An efficient parallel algorithm for DNS of buoyancy-driven turbulent flows. *J. Hydrodyn.* **31** (6), 1159–1169.

ZHOU, Q. & XIA, K.Q. 2013 Thermal boundary layer structure in turbulent Rayleigh–Bénard convection in a rectangular cell. *J. Fluid Mech.* **721**, 199–224.

ZHU, X.J., STEVENS, R.J.A.M., SHISHKINA, O., VERZICCO, R. & LOHSE, D. 2019 $Nu \sim Ra^{1/2}$ scaling enabled by multiscale wall roughness in Rayleigh–Bénard turbulence. *J. Fluid Mech.* **869**, R4.

ZHU, X.J., STEVENS, R.J.A.M., VERZICCO, R. & LOHSE, D. 2017 Roughness-facilitated local 1/2 scaling does not imply the onset of the ultimate regime of thermal convection. *Phys. Rev. Lett.* **119** (15), 154501.

ZONTA, F. & SOLDATI, A. 2018 Stably stratified wall-bounded turbulence. *Appl. Mech. Rev.* **70** (4), 040801.